JOM, Vol. 70, No. 6, 2018
https://doi.org/10.1007/s11837-018-2771-x

TECHNICAL COMMUNICATION

Single-Track Melt-Pool Measurements and Microstructures in Inconel 625

SUPRIYO GHOSH,[1,2] LI MA,[1] LYLE E. LEVINE,[1] RICHARD E. RICKER,[1] MARK R. STOUDT,[1] JARRED C. HEIGEL,[1] and JONATHAN E. GUYER[1]

1.—Materials Science and Engineering Division, National Institute of Standards and Technology, 100 Bureau Drive, Gaithersburg, MD 20899, USA. 2.—e-mail: gsupriyo2004@gmail.com

We use single-track laser melting experiments and simulations on Inconel 625 to estimate the dimensions and microstructure of the resulting melt pool. Our work is based on a design-of-experiments approach which uses multiple laser power and scan speed combinations. Single-track experiments generated melt pools of certain dimensions that showed reasonable agreement with our finite-element calculations. Phase-field simulations were used to predict the size and segregation of the cellular microstructure that formed along the melt-pool boundaries for the solidification conditions that changed as a function of melt-pool dimensions.

INTRODUCTION

Additive manufacturing (AM) technologies are rapidly being applied to fabricate near-full-density, high-value metallic parts for use in aerospace, medical, and defense applications.[1–3] When a laser source with given power (P) and power distribution scans at a programmed speed (V) across an alloy substrate or powder, a melt pool of certain dimensions (length l, width w, depth h) results. These dimensions are important, as they determine the density of the resulting part after subsequent solidification processes, affecting the material properties.

Measurements of melt-pool dimensions have been reported for various combinations of P and V using single-track experiments on Ni alloys,[4–6] stainless steels,[7] and Ti alloys.[8] High values of P and low values of V resulted in large melt pools in the above experiments. A thermographic camera was used to estimate the thermal history of the material, from which the melt-pool dimensions were determined.[4,9] Although the melt-pool shape was similar in both powder and substrate cases, the powder case was complicated by the surface roughness of the unmolten powder particles and by width and height variations and pore formations through keyholing events.[7,8] The molten pools that form during experiments[4,5] on an Inconel 625 (IN625) surface become fully developed and reach a steady state for a single-line laser scan after the first 1 mm to 2 mm. However, when experiments were performed with multiple laser scans, the melt-pool length deviated from the steady state as the scan line count was increased.[5] Therefore, a single-track laser scan on a bare IN625 substrate is used for validation simulations.

The interaction between the laser beam and irradiated material can be very complex,[2,10,11] leading to rapid vaporization of the melt surface under the beam, which results in recoil pressure coupled with Marangoni and other hydrodynamic effects within the melt pool,[2,10,11] determining the steady-state melt-pool dimensions in real systems. Modeling of such a multiphysics phenomenon is extremely difficult using feasible computational time and resources. Therefore, laser melting processes with a relatively low-power beam are often modeled using finite-element methods with simplified assumptions of the melt-pool dynamics, to simplify the calculations without any qualitative change in the resultant melt-pool shape.[6,12,13]

The shape of a melt pool is important from a solidification perspective. Solidification begins at the trailing edge of a melt pool, and the temperature gradient G and solid–liquid interface growth rate R change as a function of the melt-pool dimensions. A rapid solidification condition[14,15] is reported[16,17] to exist along the melt-pool boundary, and the resultant local solidification features, such as grain size and solute distribution, deviate increasingly from local equilibrium with increasing G and R

(Published online February 20, 2018)

combinations.[13,18] There have been no studies aimed at understanding single-track melting, solidification, and microstructure evolution phenomena in IN625. Modeling of melt pool dimensions and microstructure based on the design-of-experiments approach[4,8,19] could potentially be used for rapid optimization of P and V combinations to produce high-fidelity parts, saving significant time and cost compared with conducting numerous physical experiments. We present herein single-track laser experiments to determine melt-pool shapes, finite-element simulations to predict melt-pool shapes and temperatures, and phase-field simulations to reveal melt-pool solidification microstructures.

MELT-POOL SHAPE

Single-Track Experiments

Well-separated, single laser tracks on a solid IN625 plate were produced using a commercial laser powder bed fusion (LPBF) machine with a Nd:YAG laser. The IN625 plate had approximate dimensions of 25.4 mm × 25.4 mm × 3.2 mm. The plate was polished to controlled surface finish (400 grit) and annealed at 870°C for 1 h in vacuum to relieve residual stresses. Seven laser tracks were produced, each 4 mm long, using different combinations of P and V. The dynamic length of the melt pools was measured in situ using thermography, as reported and described previously.[4] The width of the laser tracks was measured ex situ by confocal laser scanning microscopy (CLSM). The laser tracks were cross-sectioned at the center positions (after the melt pool reached a steady-state length) and polished prior to chemical etching with aqua regia. These cross-sections were then imaged using the same CLSM setup.

Figure 1 shows CLSM images of the laser track cross-sections as a function of P and V. Clearly, the cross-section geometry was highly sensitive to both P and V. Except for the laser track formed using 195 W and 200 mm s^{-1} (case 5), the cross-sections exhibited straightforward systematic changes with respect to both P and V. The cross-section in case 5 had a different shape, indicative of onset of keyholing. Another case worth mentioning is case 7, with 195 W and 800 mm s^{-1}. These are the nominal settings used for building solid components from IN625 powder for the LPBF machine used in this study. The measured melt-pool width (w) and depth (h) are listed below each image. The standard deviation measurement uncertainties for w and h are approximately 1 μm. The uncertainties in the melt-pool length are described in Ref. 4 and shown graphically in Fig. 2.

Finite-Element Simulations

We performed heat-transfer-based finite-element simulations and validated the resulting melt-pool dimensions and temperature distributions using the above experiments.[4,5] Similar to the experiments,[4,5] a single-track laser scan on a solid IN625 substrate with dimensions of 25.4 mm × 25.4 mm × 3.2 mm at initial uniform temperature of 293 K was modeled. The laser beam was modeled as having a Gaussian power distribution with $1/e^2$ radius of 70 μm,[20] scanned at a velocity V along a length of 4 mm. Seven combinations of P (49 W to 195 W) and V (200 m s^{-1} to 800 m s^{-1}) were applied in the simulations, which were based on LPBF measurements.[4,5] The finite-element thermal model and surface laser heat input were based on our previous works.[17,19] We consider the bulk material properties from Refs. 17 and 19 with no powder material or melt-state change considered. As a first approximation, the thermal conductivity was treated as a function of temperature only.[17] The temperature-dependent bulk material density, latent heat, and specific heat were calculated thermodynamically.[17] For more details, refer to Refs. 17 and 19.

Although not shown here, the temperature was maximum at the top surface of the melt pool and varied along the melt pool length, width, and height. The leading edge (in the length direction) of the melt pool close to the laser was wide, while the trailing edge of the melt pool was narrow, as the material cools with increasing distance from the laser, consistent with experiments.[4,5] The periphery of such a typical melt-pool shape is given by the solidus temperature (1587 K) isotherm for IN625, from which we extracted the melt-pool dimensions (Fig. 1). The melt-pool length typically stabilized after 2 mm from the start of the laser scan in our simulations, reaching a steady-state value. Figure 2 presents the simulated melt-pool length measured between 195 μm and 910 μm at steady state, which

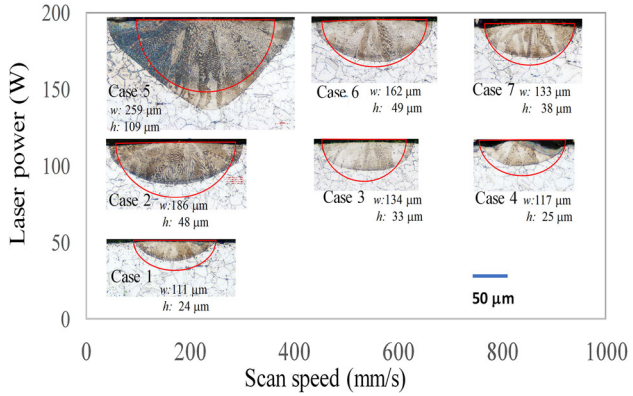

Fig. 1. Dimensions (w and h) of the melt pool that formed during experiments, measured from transverse cross-sections of laser tracks. Results are presented for seven combinations of P (49 W, 122 W and 195 W) and V (200 mm s^{-1}, 500 mm s^{-1}, 800 mm s^{-1}). Both w and h increased with increasing P for constant V, while they both decreased with increasing V for constant P. The corresponding melt-pool boundary from finite-element simulations was approximated by the solidus temperature isotherm (shown in red) and is overlaid on the experimental images for representation.

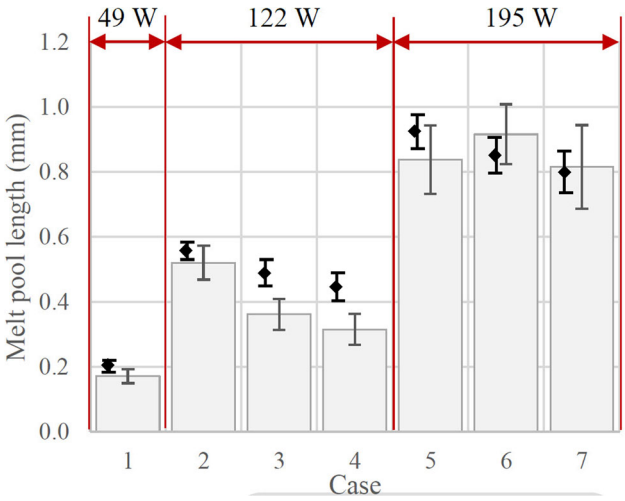

Fig. 2. Comparison of melt-pool length between experiments (columns) and simulations (diamonds) for seven cases. Experimental uncertainties (error bars) reflect the standard deviation variability of melt-pool length in steady-state conditions.[4] The uncertainties in the simulated melt-pool lengths reflect the solidus or liquidus transition of IN625. For most cases, simulated melt-pool lengths lie within experimental uncertainties.[4]

compares reasonably to length values from experiments.[4] The melt-pool length increased as the laser power was increased, and decreased similarly as the beam speed was increased, consistent with experimental observations.[4] The melt-pool length was only 5% smaller compared with the experimental value when using 195 W and 800 mm s^{-1} (case 7), well within experimental uncertainties.

Next, we present width and height measurements of the melt-pool cross-section having maximum depth in the build direction (Fig. 1). Consistent with our experiments, both w and h increased with increasing P for constant V and decreased with increasing V for constant P; w varied between 120 μm and 180 μm, whereas h varied between 38 μm and 88 μm. The calculated w is within 2% of the experimental value with $V = 800\text{mm s}^{-1}$. Combining the measurements of l and w, on average, the simulated l/w ratios lie within 6% of the experimental measurements.

The model systematically overpredicted the melt-pool depth for all cases (except case 5), which is presumably due to the use of a high laser absorptivity ($\eta = 0.5$) in our simulations.[2,11] The model underpredicted the width and depth and produced an incorrect melt-pool shape for case 5, which can be attributed to complex melt-pool dynamics, such as surface tension and recoil pressure, which we did not include in the model as a first approximation. Case 5 corresponds to the onset of keyholing in experiments,[4,5] in which a topological depression is formed owing to vaporization of material under high energy input and the melt pool becoming V-shaped.

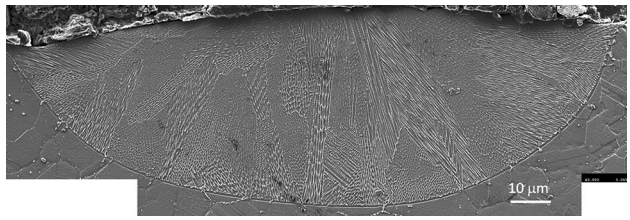

Fig. 3. SEM image of transverse cross-section of the melt pool for case 7 (Fig. 1). On average, the cellular dendritic microstructural features evolve roughly perpendicular to the melt-pool boundary in the direction of the temperature gradient.

MELT-POOL SOLIDIFICATION

Experimental Microstructures

Scanning electron microscopy (SEM) analysis with standard metallographic techniques[21] was used to reveal the microstructure of the solidified melt pool for 195 W and 800mm s^{-1} (case 7). The initial solid–liquid interface can be easily distinguished in Fig. 3, evolving primarily into cellular dendritic microstructure at steady state. On average, the microstructure is coarse close to the bottom and fine close to the rear of the solidified melt-pool interface.[1,16,18] The individual cellular grains with distinct misorientations predominantly grow throughout the melt pool, which are often observed to solidify in the same misorientation during multitrack solidification.[1,16] The average spacing between the primary dendrites varies between ≈ 0.2 μm and 1.0 μm, and the average grain size consisting of dendrites having the same orientation ranges between ≈ 10 μm and 50 μm. Although not shown here, one could expect electron backscatter diffraction analysis to show strong, fine-scale microsegregation of Nb, Mo, and other elements between the dendrites.[22,23] The dendrite sizes, orientations, morphologies, and microsegregation are different at different locations within the melt pool. This is primarily due to different positions and orientations of the initial nuclei combined with different thermal gradients and solidification velocities along the melt-pool boundary. In situ measurements of these solidification conditions are difficult due to the high temperature and small volume of the melt pools, so finite-element simulations were used instead.

Solidification Parameters

Solidification parameters were extracted from the simulated temperature and velocity fields along the melt-pool dimensions. The trailing edge of the moving melt pool is the solidification front where microstructural evolution takes place. The resulting complex solid–liquid interface morphologies such as cells and dendrites can be characterized locally within the trailing edge of the melt pool based on the average temperature gradient $G = \frac{1}{N}\sum_{i=1}^{N} |\nabla T_i(l, w, h)|$ and

average solidification rate $R = \frac{1}{N}\sum_{i=1}^{N} V\cos\alpha_i(l,w,h)$, where N is the number of elements present between the bottom and rear of the melt pool along the solidification front, T_i is the temperature, and α_i is the solidification angle at element i.[18] Both G and R vary as a function of the melt-pool dimensions. Note that both G and R increase as the melt pool becomes smaller with increasing V (Fig. 4). On the other hand, G decreases as the melt pools become larger with increasing P for constant V. On average, G is minimum (0.6×10^7 K m^{-1}) for the largest melt pool (case 5) and maximum (1.5×10^7 K m^{-1}) for the smallest melt pool (case 1). As expected, R is minimum (0.05 m s^{-1}) for the cases with smallest V and maximum (0.2 m s^{-1}) for the cases with largest V.

Phase-Field Simulations

With the preceding calculations of the melt-pool parameters, it is now possible to model the solidification process in the melt pool. We used a binary alloy phase-field model[24] to simulate γ-Ni cells and microsegregation of Nb (nominal mass fraction 4%) as a binary approximation of the IN625 microstructure. The time-dependent order parameter (ϕ) and concentration (c) model equations of motion were solved on a uniform mesh (480×5000), using the finite-volume method, explicit time-stepping scheme, and zero-flux boundary conditions. Since solid–liquid interface equilibrium does not hold during AM solidification,[18] the present simulations were conducted for vanishing antitrapping solute flux term (second term inside bracket in Eq. 5 in Refs. 17 and 18) to model realistic solute redistribution across the solid–liquid interfaces. The original purpose of adding this extra solute flux term to the standard Fickian diffusion flux in the concentration equation was to enforce local equilibrium during low-velocity casting solidification simulations.[24] The solid–liquid interfacial energy $\sigma = 0.3$ J m^{-2},[25] the solid–liquid cubic anisotropy parameter $\epsilon_4 = 0.02$,[25] and the solid–liquid interface thickness $W_0 = 5$ nm were approximated for a Ni-Nb alloy. For the model equations and other numerical and thermophysical parameters, refer to Refs. 17 and 18. Each simulation began with a thin layer of solid at the bottom of the simulation box, accompanied by a small, random amplitude perturbation in ϕ at the initial solid–liquid interface, from which stable perturbations grew with time and broke into steady-state γ-Ni cells (Fig. 4).

The microstructures that form during laser resolidification are governed by the combination of G and R. The ratio G/R determines the nature of the solidification front (planar, cellular or dendritic), whereas the product GR (cooling rate) controls the size of the solidification structure.[14,15] In our finite-element calculations, G/R varies between 80 K s mm^{-2} and 300 K s mm^{-2} whereas GR varies between 3×10^6 K s^{-1} and 3×10^7 K s^{-1}. In this G–R space, our simulations predict columnar dendritic morphology of the Ni-rich γ matrix phase. The average distance between the γ cells remains constant at steady state (Fig. 4), being the primary dendrite arm spacing λ. We used Fourier spectrum analysis[26] of the solid–liquid interface of the cellular microstructures to estimate λ. In our simulations, λ decreased with increasing GR, ranging between 0.20 μm and 0.43 μm, which can be approximated following Hunt[27] as $\lambda\,(\mu\text{m}) = A(k\Gamma T_0 D_l)^{0.25} G^{-0.5} R^{-0.25}$, where k is the partition coefficient, Γ is the Gibbs–Thomson coefficient, T_0 is the equilibrium freezing range, D_l is the diffusivity of the liquid, and the coefficient A is calculated to lie between 0.13 and 0.17. Such extremely dense cellular microstructures improve the yield and tensile and fatigue strengths of the as-deposited material and reduce melt flow effects.[28] λ decreases significantly with increasing V, while λ does not seem to be affected by increasing P in our simulations.

Niobium is the most important alloying element in IN625. Niobium segregates most severely from the solid cell core (c_s) to the liquid (c_l) as it has the smallest equilibrium partition coefficient ($k = c_s/c_l = 0.48$) among all elements in IN625, and determines the solidification pathways and precipitation of strengthening phases in the solid state.[29] Our simulations show strong microsegregation of Nb in between the cells, illustrating the occurrence of nonequilibrium Nb redistribution during single-line laser resolidification. As a result, k becomes a function of the solid–liquid interface growth rate R and ranges between $0.58 \le k \le 0.72$ (Fig. 4). Note that the limit $k = 1$ is reportedly

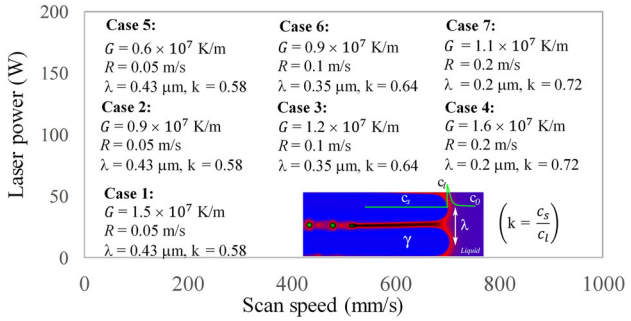

Fig. 4. Snapshot of typical cellular microstructure at steady state for 195 W and 800 mm s^{-1} (bottom right). Two main features of the γ cells are reported, viz. the primary spacing λ and the Nb distribution coefficient k, as functions of the average temperature gradient G and solidification rate R. λ decreases by almost 20% as R increases by a factor of 2. The cell core composition c_s (3.7%) remains constant as the diffusivity of solid is ignored. Since Nb is rejected as the cells grow, there is a spike in the Nb composition c_l (5.1%), which decays exponentially to reach the nominal composition c_0 (4.0%) in the far-field liquid. The distribution of Nb across the cell–liquid interface is thus represented by the nonequilibrium distribution coefficient $k = c_s/c_l$. Similar to λ, the effect of P is negligible on k, which increases with increasing V. k deviates by 50% from the local equilibrium ($k = 0.48$) for the cases with highest V.

reached only at $R \geq 9\,\mathrm{m\,s^{-1}}$.[30] In contrast to λ, k increases significantly with increasing R (or V), while k does not seem to be affected by increasing P. Such a response of the solidifying Ni-Nb melt pool boundary due to laser treatment can be characterized using the Aziz[31] solute-trapping function given by $k = (1 + R/V_d)/(0.48 + R/V_d)$, where $V_d = 0.23\ \mathrm{m\ s^{-1}}$ is the diffusion velocity of Nb during laser resolidification in IN625. The Nb-rich liquid droplets (Fig. 4) that shed from the root region of the dendrites subsequently freeze, leading to regions of highest microsegregation which could transform to intermetallic phases in the solid state.[22]

DISCUSSION AND CONCLUSION

We used experimental measurements of the melt-pool dimensions (l, w, and h) to validate heat-conduction-based finite-element simulations for the $P - V$ map of single-track laser treatments. The size of the melt pool increased with increasing P and decreasing V. Our simulations showed a reasonable match of l, w, h, and l/w with experiments, except when keyhole melting was observed experimentally. The l/w ratio calculated in this case was 3.2, close to the value when the melt-pool dimensions become a function of surface tension, recoil pressure, and other hydrodynamic effects[2,7] that affect the shape and stability of the keyhole. The laser absorptivity also becomes an increasing function of the beam power, which we model as a constant ($\eta = 0.5$) for simplification reasons. Note that keyhole solidification often results in porosity, leading to poor mechanical behavior of the parts, and is therefore not recommended for AM processing.[6,32] The finite-element simulations in Ref. 33 are particularly interesting in that they characterize the melt-pool dynamics based on its dimensions using a high-power ($P = 500\,\mathrm{W}$) laser beam, and it was observed that the simulated melt-pool dimensions deviated increasingly from experimental measurements with increasing P. For a system with a low- to moderate-power laser beam and very small melt-pool depth ($h < 50\,\mu\mathrm{m}$), our simulations may be appropriate, as discussed in Refs. 12 and 16.

As demonstrated by multiphysics modeling of the laser–powder–substrate interaction in Ref. 2, the vaporization-induced recoil force on the melt pool typically produces a "hollow" under the laser beam that extends through the powder layer into the substrate. This is even true in the conduction regime in which additive manufacturing is typically carried out. Such behavior cannot be readily incorporated into a finite-element model, so all such models must be seen as severe approximations, and the best way we know to validate such a model is to test whether the predicted melt geometry is correct. That is the approach taken here. If the steady-state melt-pool length and cross-sectional size and shape are correct, then the resulting thermal behavior as a function of time and position should be adequate for microstructure evolution studies. One drawback to this approach is that it is only valid for one material system at a time, IN625 in this case. Also, although the current finite-element model should be adequate for the results reported here, it should be mentioned that, although the melt-pool lengths agree well with the in situ melt-pool measurements, the shapes of the melt pool are not perfect. Decreasing the absorptivity and slightly increasing the width of the laser beam would likely improve the agreement, and work in this direction is in progress along with in situ measurements of the absorptivity.[34]

The melt-pool cooling rates estimated from both experiments and simulations are on the same order of magnitude of $\approx 10^6\,\mathrm{K\,s^{-1}}$. The microstructural features that form at these cooling rates in our simulations change primarily as a function of R, signifying that R is a more important parameter than G during AM. Previous studies have shown that $G/R < 1\,\mathrm{K\,s\,mm^{-2}}$ resulted in an equiaxed mode of dendritic solidification, $1\,\mathrm{K\,s\,mm^{-2}} < G/R < 80\,\mathrm{K\,s\,mm^{-2}}$ resulted in mixed equiaxed–columnar solidification, and $G/R > 80\,\mathrm{K\,s\,mm^{-2}}$ resulted in columnar solidification in Inconel alloys.[35] In our simulations, G/R ranges between $80\,\mathrm{K\,s\,mm^{-2}}$ and $300\,\mathrm{K\,s\,mm^{-2}}$, producing columnar dendritic morphology. The $G - R$ solidification map was determined using various combinations of P and V and can therefore be used, for example, to engineer appropriate grain morphology and grain size for different sections of the AM parts. The simulations of melt-pool solidification in Ref. 36 are particularly interesting, where an initial solid–liquid interface, similar to the resolidification boundary in our Fig. 3, resulted in local nucleation and growth of multiple dendrites with misorientation from the vertical direction of 0° to 20° depending on the scan velocity, thermal gradient, interface roughness, and initial seed position.

Unlike finite-element simulations, the microstructure evolution for the calculated $G - R$ solidification map does not depend strongly on the melt-pool dynamics. This is precisely due to the extremely fine cellular structures, which provide significant resistance to fluid flow following an exponential increase of the damping effect in the semisolid mushy region.[28] Phase-field simulations performed on Ni-Nb alloys showed that the solute redistribution across dendrites remained similar when simulations were conducted with and without convection.[37] The effects of convection on the spacing between primary dendrite arms is not as pronounced compared with the spacing between side arms,[37] which we did not observe in our simulations. Therefore, melt-pool solidification is modeled with reasonable approximations for the same parameter combinations in both experiments and simulations. Further research is required for more

accurate characterization of the melt-pool dimensions and multicomponent solidification microstructures[38] with and without melt pool dynamics to improve the predictive capabilities for the quality of as-built parts, although such work would be computationally intensive.

REFERENCES

1. L.E. Murr, E. Martinez, K.N. Amato, S.M. Gaytan, J. Hernandez, D.A. Ramirez, P.W. Shindo, F. Medina, and R.B. Wicker, *J. Mater. Res. Technol.* 1(1), 42 (2012).
2. W.E. King, A.T. Anderson, R.M. Ferencz, N.E. Hodge, C. Kamath, S.A. Khairallah, and A.M. Rubenchik, *Appl. Phys. Rev.* 2(4), 041 (2015).
3. M. Francois, A. Sun, W. King, N. Henson, D. Tourret, C. Bronkhorst, N. Carlson, C. Newman, T. Haut, J. Bakosi, J. Gibbs, V. Livescu, S.V. Wiel, A. Clarke, M. Schraad, T. Blacker, H. Lim, T. Rodgers, S. Owen, F. Abdeljawad, J. Madison, A. Anderson, J.L. Fattebert, R. Ferencz, N. Hodge, S. Khairallah, and O. Walton, *Curr. Opin. Solid State Mater. Sci* 21(4), 198 (2017).
4. J.C. Heigel and B.M. Lane, Measurement of the melt pool length during single scan tracks in a commercial laser powder bed fusion process, in *MSEC*, vol. 2017 (2017).
5. J.C. Heigel and B.M. Lane, The effect of powder on cooling rate and melt pool length measurements using in situ thermographic techniques, in *Solid Freeform Fabrication Symposium*, vol. 2017 (2017).
6. C. Montgomery, J. Beuth, L. Sheridan, and N. Klingbeil, Process mapping of Inconel 625 in laser powder bed additive manufacturing, in *Solid Freeform Fabrication Symposium*, vol. 2015, 1195–1204 (2015).
7. T. Childs, C. Hauser, M. Badrossamay, *Proc. Inst. Mech. Eng., Part B J. Eng. Manuf.* 219(4), 339 (2005).
8. H. Gong, H. Gu, K. Zeng, J. Dilip, D. Pal, B. Stucker, D. Christiansen, J. Beuth, and J.J. Lewandowski, Melt pool characterization for selective laser melting of Ti-6Al-4V pre-alloyed powder, in *Solid Freeform Fabrication Symposium*, vol. 2014, pp. 256–267 (2014).
9. B. Lane, S. Moylan, E. Whitenton, and L. Ma, *Rapid Prototyp. J.* 22(5), 778 (2016).
10. W.E. King, H.D. Barth, V.M. Castillo, G.F. Gallegos, J.W. Gibbs, D.E. Hahn, C. Kamath, and A.M. Rubenchik, *J. Mater. Process. Technol.* 214(12), 2915 (2014).
11. S.A. Khairallah, A.T. Anderson, A. Rubenchik, and W.E. King, Acta Mater. 108, 36 (2016).
12. W. Guo and A. Kar, Sci. Technol. Weld. Join. 5(5), 317 (2000).
13. X. Gong and K. Chou, *JOM* 67(5), 1176 (2015).
14. W. Kurz and D.J. Fisher, *Fundamentals of Solidification* (TransTech, Zurich, Switzerland, 1998).
15. M. Rappaz, J.A. Dantzig, *Solidification* (EFPL Press, Lausanne 2009).
16. W.J. Sames, F.A. List, S. Pannala, R.R. Dehoff, and S.S. Babu, *Int. Mater. Rev.* 61(5), 315 (2016).
17. T. Keller, G. Lindwall, S. Ghosh, L. Ma, B. Lane, F. Zhang, U.R. Kattner, E.A. Lass, J.C. Heigel, Y. Idell, M.E. Williams, A.J. Allen, J.E. Guyer, and L.E. Levine, *Acta Mater.* 139, 244 (2017).
18. S. Ghosh, L. Ma, N. Ofori-Opoku, and J.E. Guyer, *Modell. Simul. Mater. Sci. Eng.* 25(6), 065 (2017).
19. L. Ma, J. Fong, B. Lane, S. Moylan, J. Fillibenm, A. Hecker, and L. Levine, Using design of experiments in finite element modeling to identify critical variables for laser powder bed fusion, in *Proceedings of the 26th Annual International Solid Freeform Fabrication Symposium: An Additive Manufacturing Conference*, pp. 219–228 (2015).
20. R. Dayal, Numerical modelling of processes governing selective laser sintering. Ph.D. thesis, Technische Universität (2014).
21. G. Vander Voort, Metallography, principles and practice. McGraw-Hill series in materials science and engineering. ASM International, Materials Park, OH, (1999).
22. F. Zhang, L.E. Levine, A.J. Allen, C.E. Campbell, E.A. Lass, S. Cheruvathur, M.R. Stoudt, M.E. Williams, and Y. Idell, *Scr. Mater.* 131, 98 (2017).
23. E.A. Lass, M.R. Stoudt, M.E. Wililiams, M. Katz, L.E. Levine, T. Phan, T. Gnaeupel-Herold, and D. Ng, *Metall. Mater. Trans. A* 48(11), 5547 (2017).
24. B. Echebarria, R. Folch, A. Karma, and M. Plapp, *Phys. Rev. E* 70(6), 061 (2004).
25. J. Hoyt, M. Asta, and A. Karma, *Mater. Sci. Eng. R Rep.* 41(6), 121 (2003).
26. M. Greenwood, M. Haataja, and N. Provatas, *Phys. Rev. Lett.* 93, 246 (2004).
27. J.D. Hunt, The Metal Society, London 3 (1979).
28. W. Tan, N.S. Bailey, and Y.C. Shin, *Comput. Mater. Sci.* 50(9), 2573 (2011).
29. F. Liu, X. Lin, H. Leng, J. Cao, Q. Liu, C. Huang, W. Huang, *Opt. Laser Technol.* 45, 330 (2013).
30. W. Kurz and R. Trivedi, *Mater. Sci. Eng. A* 179, 46 (1994).
31. M.J. Aziz, *J. Appl. Phys.* 53(2), 1158 (1982).
32. R. Rai, J.W. Elmer, T.A. Palmer, and T. DebRoy, *J. Phys. D Appl. Phys.* 40(18), 5753 (2007).
33. J.I. Arrizubieta, A. Lamikiz, F. Klocke, S. Martínez, K. Arntz, and E. Ukar, *Int. J. Heat Mass Transf.* 115, 80 (2017).
34. M. Matthews, Private communication (2017).
35. N. Raghavan, R. Dehoff, S. Pannala, S. Simunovic, M. Kirka, J. Turner, N. Carlson, and S.S. Babu, *Acta Mater.* 112, 303 (2016).
36. R. Acharya, J.A. Sharon, and A. Staroselsky, *Acta Mater.* 124, 360 (2017).
37. L. Yuan and P.D. Lee, *Model. Simul. Mater. Sci. Eng.* 18(5), 055 (2010).
38. S. Ghosh and M. Plapp, *Acta Mater.* 140, 140 (2017).